

Full paper

Visualizing ion diffusion in battery systems by fluorescence microscopy: A case study on the dissolution of LiMn_2O_4

Yali Qiao^a, Zhi Zhou^{a,b}, Zhixing Chen^c, Sicen Du^a, Qian Cheng^a, Haowei Zhai^a,
Nathan Joseph Fritz^a, Qiang Du^a, Yuan Yang^{a,*}

^a Department of Applied Physics and Applied Mathematics, Columbia University, New York, NY 10027, United States

^b Department of Applied Mathematics, The Hong Kong Polytechnic University, Kowloon, Hong Kong, China

^c Department of Chemistry, Stanford University, Stanford, CA 94305, United States

ARTICLE INFO

Keywords:

Fluorescence imaging
 LiMn_2O_4 cathode
Ion dissolution and diffusion
Batteries

ABSTRACT

Fundamental understanding of ionic transport is critical to developing rechargeable batteries with high performance. While various techniques have been developed to characterize ionic transport in solid battery electrodes, little has been done to visualize ion movement in the liquid electrolyte, since it is difficult to realize high temporal, spatial and concentration resolutions simultaneously in liquids. Fluorescence imaging has the capability to detect ions in liquid with high resolution (< 1 s, < 300 nm and < 1 M), and it is widely used in biomedical studies. However, it has been rarely applied to battery studies. Here we show that using an ion indicator, the dissolution of trace amount of Mn from LiMn_2O_4 , a common Li-ion battery cathode material, can be visualized under a fluorescence microscope. Moreover, important physical parameters, such as the dissolution rate and ionic diffusivity, can be extracted quantitatively from the fluorescence images. These results also show that nanoscale Al_2O_3 coating can effectively suppress Mn dissolution, which is consistent with past studies. This study demonstrates the capability of fluorescence-imaging based techniques for battery studies, which could help gain more insight on the behavior of ions in battery systems and develop better battery materials.

1. Introduction

High-performance batteries are essential to applications ranging from portable electronics to vehicle electrification and grid-level energy storage [1–4]. Visualization of electrochemical/chemical processes in batteries is critical to understanding the underlying mechanisms and transforming battery technologies. The electrode materials and the electrolyte are two major components in batteries. Recently, various tools [5] have been developed to characterize solid electrodes (e.g. ion transport and phase transformation) with unprecedented resolutions, such as X-ray imaging [6–12], electron microscopy [13–16] and scanning probe microscopies [17–19]. However, few studies have been reported on visualizing ion transport in the liquid electrolyte [20], which also plays an important role in battery performance. For example, inhomogeneities in ionic flux can reduce power density and promote the growth of Li dendrites [21]. There are multiple challenges to imaging ions in the liquid phase: 1) their concentrations (< 0.1 – 1 M) are typically much lower than that in the solid phase (~ 10 M). Such concentration is at or below the detection limit of many electron and X-ray-based techniques (e.g. EDS), 2) Ion diffusion in a liquid is typically

much faster than that in a solid (10^{-5} – 10^{-6} cm^2/s vs. $< 10^{-8}$ cm^2/s), which homogenizes ion distribution. Therefore, shorter time scales (e.g. < 1 s) and higher resolution in concentration are needed in detection, and 3) many important ions in battery systems (e.g. Li^+ , Na^+ , Mn^{2+}) have low absorption in the visible and infrared spectrum, which makes direct optical methods unsuitable for characterization. Therefore, most approaches to imaging solid electrodes are difficult to characterize ions in liquid with high spatial, temporal and concentration resolutions simultaneously (e.g. < 1 μm , < 1 s and < 1 mM).

On the other hand, fluorescence-based imaging can visualize trace amount of ions in liquid with ultrahigh resolution (< 300 nm, < 50 ms and < 0.1 μM), and the spatial resolution could be further enhanced to ~ 10 nm in the super-resolution mode [22,23]. This technique is based on the “turned on” fluorescence emission of a fluorescence dye when it binds selectively to a certain ion. Fluorescence-based imaging has been widely used in biomedical studies (e.g. neuron imaging [24]), and also in studies on catalysts [25–27]. However, they are rarely applied to battery studies. Only two examples are reported in literature. Recently Kostecki et al. [28] reported the fluorescence imaging of the solid electrolyte interphase on a graphite electrode and its relation to Mn

* Corresponding author.

E-mail address: yy2664@columbia.edu (Y. Yang).

dissolution from $\text{LiNi}_{0.5}\text{Mn}_{1.5}\text{O}_4$. Goldsmith et al. [20] investigated the real-time tracking of lithium ions via widefield fluorescence microscopy, which enables quantitative determination of the lithium ion diffusion constant, in a microfluidic model system for a plasticized polymer electrolyte. Besides, very recently, White et al. [29] reported a quite interesting work on introducing UV–vis spectrum for the first time as an in-operando experimental technique to detect the concentration of Mn^{2+} ions from manganese(II) acetylacetonate ($\text{Mn}(\text{acac})_2$) in electrolyte based on a UV–vis probe molecule (4-(2-pyridylazo) resorcinol, PAR) and activator (1,8-bis(dimethylamino)naphthalene, proton sponge) combination. Here we use the dissolution of Mn ions from LiMn_2O_4 (LMO) in an acidic aqueous solution as an example to demonstrate the capability of fluorescence imaging of electrolytes, a case directly relevant to battery systems.

LMO is a cathode material for rechargeable Li-ion batteries with both aqueous [30–33] and organic electrolytes [34]. It is attractive as it has low-cost and high power capability [35–37]. However, it is well known to have a limited cycle life due to the dissolution of Mn ions in battery electrolyte, especially at high temperature [38,39]. The process is as follows [38–40]: 1) the trace amount of water (20–100 ppm) in the electrolyte reacts with LiPF_6 to generate HF, 2) H^+ in HF attacks LMO and Mn^{3+} is dissolved in the electrolyte, and 3) Mn^{3+} disproportionates to Mn^{2+} and Mn^{4+} . ICP-AES has been widely used to study the temporal evolution of Mn ions dissolved in the electrolyte. However, this method can only provide average information over the whole electrode. It cannot answer detailed questions such as whether there is any particle-to-particle inhomogeneity in the dissolution, and how Mn ions diffuse in the electrolyte. To address this challenge here, we report the use of fluorescence imaging to visualize the dissolution and diffusion process of Mn ions from LMO (Fig. 1). As a proof-of-concept, we studied the dissolution and one dimensional (1D) diffusion of Mn ions in an aqueous electrolyte, which shares the same mechanism of Mn dissolution in organic electrolyte. Slightly acidic aqueous electrolyte (pH = 5) was used in our studies. The spatial/temporal variations of fluorescence intensity provided information about the dissolution rate of Mn ions and the ion diffusivity of Mn-dye complex in the electrolyte. Besides monitoring ionic transport, the fluorescence imaging also revealed that a nanoscale Al_2O_3 coating on LMO can effectively suppress Mn dissolution and improve its electrochemical performance. Modeling and simulations were also carried out to demonstrate that the fluorescence analysis can capture the process quantitatively. The dissolution of Mn represents a model system to attest to the power of fluorescence imaging for battery systems.

2. Materials and methods

2.1. Materials and characterizations

Calcium Green™-5N (CG-5N) was purchased from Fisher Scientific. LMO was sourced from MTI. The lithium metal foil was acquired from Alfa Aesar. Other chemicals were purchased from Sigma Aldrich. Timical Super C45 carbon black and Kynar HSV900 poly(vinylidene fluoride) (PVDF) were used as-received. Scanning electron microscopy (SEM) was performed using FEI Helios NanoLab 660. The fluorescence intensity was recorded using a BioTek instrument. The fluorescence imaging was performed with a Leica TCS SP5-MP Confocal/2-Photon microscope. TEM and energy-dispersive X-ray spectroscopy (EDS) were measured using Talos F200X.

2.2. Synthesis of Al_2O_3 -coated LMO

The synthesis of Al_2O_3 -coated LMO was achieved by a sol-gel approach. Typically a precursor solution of Al_2O_3 was prepared by mixing 2.9 mmol citric acid, 5.7 mmol ethylene glycol and 1.5 mmol $\text{Al}(\text{NO}_3)_3 \cdot 9\text{H}_2\text{O}$ in 2 mL of ethanol. A mixture of 1.3 mL of precursor solution and 2.5 g LMO was dissolved in 1.3 mL of ethanol, stirred for 5 min and sonicated for 5 min. The stirring and sonicating process was repeated several times. The mixture was then heated at 50 °C in a water bath until the solvent was almost dry, heated at 80 °C for 30 min, and heated at 120 °C for another 30 min. The mixture was finally sintered at 600 °C for 3 h under air to achieve 2 wt% Al_2O_3 -coated LMO powders.

2.3. Fluorescence imaging and quantitative analysis

The glass slides used as the substrate and cover slips for fluorescence imaging were thoroughly cleaned before use in order to eliminate the interference of surface residual ions and other impurities to the fluorescence characterization. Typically, the glass slides and cover slips were first immersed in a saturated KOH solution in DI water, sonicated for 30 min, washed by DI water several times, soaked in 2 mM solution of EDTA in DI water overnight, then washed again by DI water several times. The film samples for fluorescence imaging were prepared by drop-casting a slurry of 95 wt% active cathode materials and 5 wt% PVDF binder in NMP onto a glass slide by a pipette. These were then dried at 50–60 °C for 2–3 h to remove the residual solvent.

The image processing and quantitative analysis was performed using the standard LAS AF software package offered by the system manufacturer, Leica. In order to achieve consistent quantification and high reproducibility of the data for different samples, fluorescence

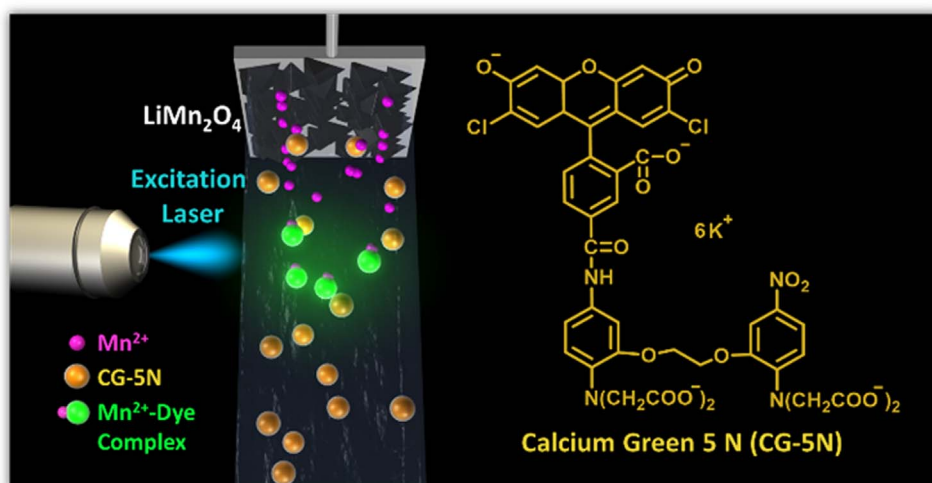


Fig. 1. Scheme of visualizing ion diffusion in battery systems by fluorescence microscopy. In the case of LiMn_2O_4 as cathode material in an aqueous model battery system, Mn^{2+} ions continuously dissolve out then diffuse into the electrolyte from the electrode/electrolyte interface. This is followed by coordination with CG-5N indicator to induce turn-on fluorescence.

visualization was performed using standardized parameters: 488 nm as excitation wavelength with an output power of the laser at 15% to detect the association of CG-5N and Mn^{2+} , emission filters of 525–555 nm, video acquisition duration of 30 min with a time interval of 2 s. The recording starts at 12 s after the addition of aqueous dye solution, due to an operation delay. The gain is kept at 900 for all the analyzed images. All images were focused and recorded using a Leica DM6000 objective.

2.4. Electrochemical characterization

The electrodes for electrochemical studies were prepared from a slurry of 75 wt% LMO active material, 15 wt% conductive carbon black, and 10 wt% PVDF binder in NMP as the solvent, which was casted onto an aluminum foil using a doctor blade and dried at 120 °C overnight. The electrochemical performance of LMO was investigated inside a pouch cell assembled in an argon-filled glovebox (oxygen and water contents below 1 and 0.1 ppm, respectively). Lithium metal foil was used as the anode. The typical cathode loading was 2–3 mg/cm². A 1 M solution of LiPF_6 in ethylene carbonate/diethyl carbonate (EC/DEC, 1:1 v/v) (Selecliyte LP40) was used as the electrolyte with a Celgard 2321 triple-layer polypropylene-based (polypropylene-polyethylene-polypropylene, MTI) membrane as the separator. Galvanostatic cycling was performed in a pouch cell using either a Bio-Logic VMP3 battery tester or a Landt Battery tester. The charge/discharge cycles were performed at different rates between 3.5 and 4.3 V at 60 °C.

3. Results and discussion

To visualize Mn^{2+} ions in aqueous solution, the first step is to identify a dye that is sensitive to Mn^{2+} , but not other ions involved in the system (e.g. Li^+ and Al^{3+}). As there is no commercially available dye specifically designed for Mn^{2+} , a calcium dye (CG-5N) was used, which also showed prompt response to Mn^{2+} , but not other ions present in this system (e.g. Li^+ and Al^{3+} ions). The response of CG-5N to Mn^{2+} is shown in Fig. 2a. When no Mn^{2+} was added, 20 μM aqueous solution of CG-5N showed a fluorescence background which peaked at 535 nm with a peak intensity (a.u.) of 8.3×10^3 . After 5, 10 and 20 μM Mn^{2+} was added, the fluorescence intensity remarkably increased to 3.01×10^4 , 5.47×10^4 and 7.57×10^4 , respectively. The fluorescence was so strong that it could be observed by the naked eye (Fig. 2a inset). These results show that fluorescence of CG-5N dye is highly sensitive to Mn^{2+} . In contrast, as shown in Fig. 2b, when 20 μM Li^+ or Al^{3+} was added, the fluorescence intensity only increased to 8.7×10^3 or 1.36×10^4 at 535 nm, respectively, indicating a good selectivity to Mn^{2+} over Li^+ and Al^{3+} . The fluorescence intensity is linear with Mn^{2+} concentration when $[\text{Mn}^{2+}]$ was smaller than [CG-5N]. However, when $[\text{Mn}^{2+}]$ was higher than [CG-5N], the signal is saturated, suggesting that all CG-5N bound to Mn^{2+} . As shown in Fig. 2b, fitting shows that the dissociation constant (K_d) was only 0.054 μM for [CG-5N] with Mn^{2+} , which proves that Mn^{2+} binds to CG-5N readily (K_d is 14 μM for [CG-5N] with calcium ion). Fitting details can be found in the Supporting information.

Because fluorescence intensity is affected by pH, and pH varies slightly (e.g. 5–7.2 over 60 min) during the dissolution of LMO, the influence of pH on fluorescence intensity was also investigated. As shown in Fig. 2c, when pH changed from 7 to 5, the maximum fluorescence intensity with saturated $[\text{Mn}^{2+}]$ only decreased marginally (~6%). When further reduced to a pH of 4.7, the intensity decreased about 30%, and the fluorescence completely vanished at pH of 3. Such results are consistent with the mild acidity of carboxylic acids with a pKa of 4.8–5 [41]. In CG-5N, multidentate coordination groups, including carboxylate, and amine nitrogen donors, are complexing with Mn^{2+} to induce fluorescence [42,43]. When the pH is less than 4.7, the carboxylate groups are partially protonated, leading to reduced

fluorescence. Therefore, a pH of 5 was chosen in our experiments, so that the pH change during the dissolution process (5–7.2) would not affect our quantitative analysis in the following discussions. The strong signal and linear relationship between fluorescence intensity and $[\text{Mn}^{2+}]$ when $[\text{Mn}^{2+}]$ was less than [CG-5N] also indicates that quantitative information can be derived from fluorescence imaging to analyze the transport behavior of ions.

The dissolution of Mn^{2+} was first monitored by a fluorometer to understand its temporal evolution. Two kinds of samples were studied. One consisted of bare LMO particles with an average size of < 5 μm (MTI corp, Fig. 3a), and the other was 2 wt% Al_2O_3 -coated LMO (Fig. 3b), which was prepared as described in the experimental section. The Al_2O_3 coating was achieved successfully (Figs. 3c–f, and S1) with a coating thickness of tens of nanometers (Fig. S2). Nanoscale porous Al_2O_3 was also observed among LMO particles (Fig. 3b). To measure the dissolution of Mn ions by fluorescence, 2 mg of each sample were soaked in a 100 μL water solution with 20 μM dye at pH = 5, and their fluorescence intensity were recorded at different times. As shown in Fig. 2d, the concentration of dissolved Mn^{2+} in both samples increased continuously with time, and bare LMO exhibited higher dissolution rate than that of the Al_2O_3 -coated LMO. Such observation is consistent with past studies that an Al_2O_3 coating on LMO could effectively suppress the dissolution of LMO in the electrolyte [44,45]. The fluorescent signal of the Al_2O_3 -coated LMO begins to saturate at around 40 min, while that of bare LMO continuously increases up to 60 min (Fig. 2d). In Fig. 2d, the fluorescence intensity (Fig. S3) is converted to Mn^{2+} concentration based on the fitting curve in Fig. 2b.

The studies above validated that the dissolution of Mn^{2+} can be monitored by fluorescence. Next the dissolution process was imaged by a fluorescence microscope to visualize its temporal and spatial evolution. In a typical experiment, 2 μL of NMP solution with 95 wt% of LMO and 5 wt% of PVDF binder was drop cast onto a pre-cleaned glass slide to form a LMO film inside an imaging spacer. Then ~ 7.5 μL of a CG-5N water solution with pH of 5 was dropped onto the film by a micro-pipette (Fig. S4). Fluorescence images were recorded near the edge of LMO film with an interval of 2 s. The excitation wavelength is 488 nm and integrated signal in the range of 525–555 nm is recorded. Fig. 4 shows corresponding fluorescence images at times of 12 s, 20 s, 40 s, 70 s, 130 s, and 610 s for LMO (Fig. 4a) and Al_2O_3 -coated LMO (Fig. 4b), respectively. At the beginning, the region near the edge of the LMO clearly showed a high fluorescence intensity while the intensity is low far away from the edge. As the time elapsed, the fluorescence intensity increased over all areas and also became more uniform, since more and more Mn is dissolved and diffuses out. In contrast, although the Al_2O_3 -coated sample prepared and imaged with the same method showed similar spatial and temporal evolution of fluorescence signals, the fluorescence intensity was much lower and the intensity increased much slower, indicating that Mn was dissolved at a much slower rate. This is consistent with results from fluorometer (Fig. 2d). To quantitatively profile the temporal and spatial distribution, fluorescence intensities at different locations and times were plotted in Fig. 4b and d for bare LMO and Al_2O_3 -coated LMO, respectively. Expectedly, the fluorescence intensity increased at all locations due to continuous dissolution of Mn^{2+} and the diffusion of ions. Moreover, nanoscale Al_2O_3 protected the LMO and thus the fluorescence intensity did not increase as fast as the bare LMO sample.

Besides studying the effect of coating, the effect of state of charge (SOC) on the Mn dissolution process, was also investigated via this fluorescence-based technique. Particularly, a LMO film that was charged to 4.3 V in a pouch cell, was well studied via fluorescence imaging. As shown in Fig. S5, the fluorescence intensity is at similar level to that of background for static LMO and coated LMO samples, indicating that there is almost no fluorescence signal of Mn-dye complex. This result is consistent with the fact that there is almost no Mn^{3+} dissolution from MnO_2 . We would like to emphasize that such spatial information could not be extracted by other techniques such as atomic

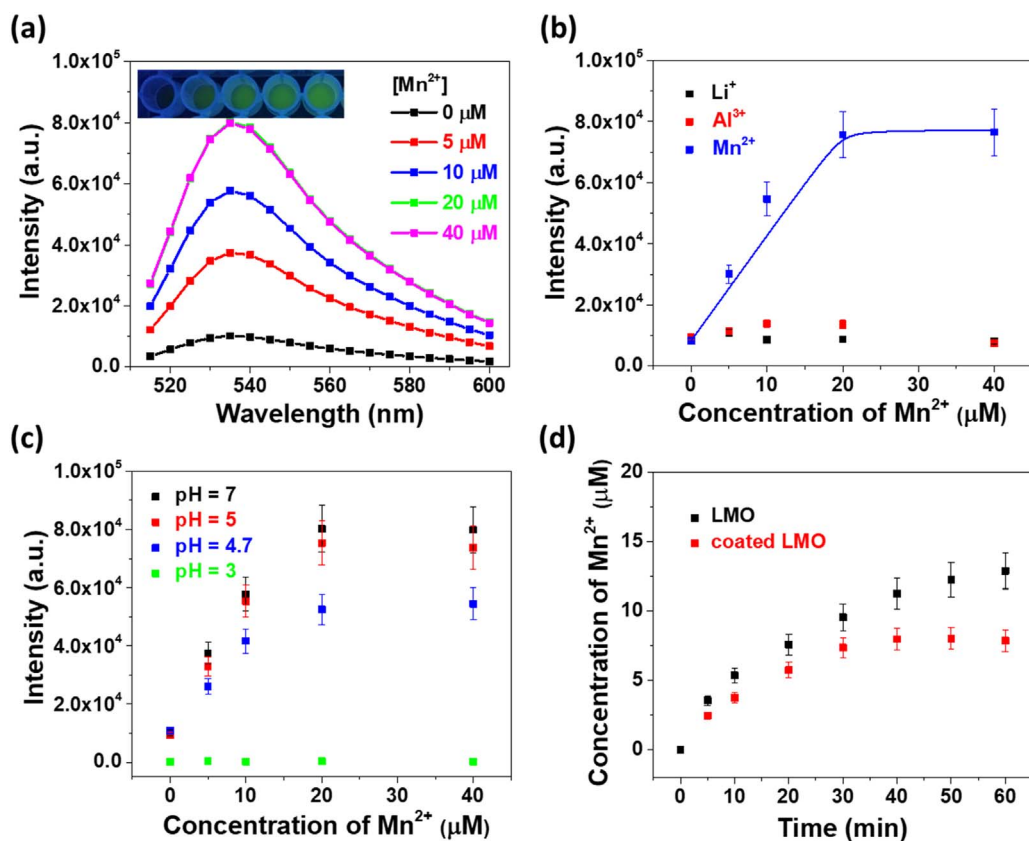


Fig. 2. Fluorescence intensity of Mn²⁺ with CG-5N dye (20 μM), monitored with an excitation wavelength of 488 nm. (a) In the presence of a range of free Mn²⁺ ion concentrations. The inset shows the increase of fluorescence intensity with [Mn²⁺]. (b) Fluorescence intensity of various ions. The solid line shows the fitted curve with $K_d = 0.054 \mu\text{M}$ ($r = 0.981$). (c) Effects of pH. A strong fluorescence signal and linear relationship with [Mn²⁺] exist at a pH between 5 and 7, where quantitative information can be derived. (d) *In-situ* dissolution of Mn ions for bare LMO and Al₂O₃-coated LMO particles at pH = 5.

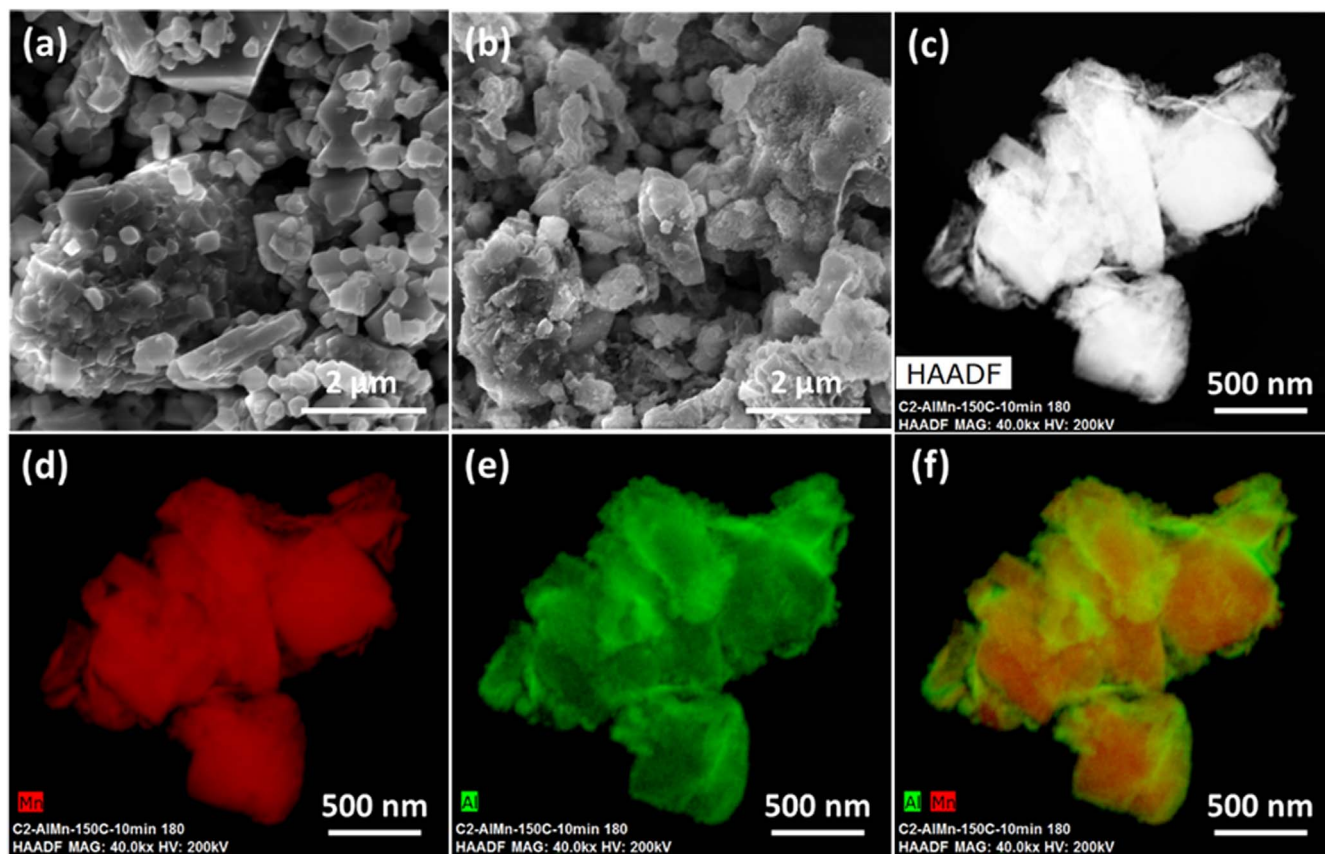


Fig. 3. Morphology of bare and coated LMO particles. SEM of (a) bare LMO, and (b) Al₂O₃-coated LMO. The size of particles is less than 5 μm. (c–f) Elemental mapping of coated LMO particles by energy-dispersive X-ray spectroscopy (EDS). (c) High angle annular dark field (HAADF) image, (d) Mn (e) Al, and (f) overlap of Mn and Al.

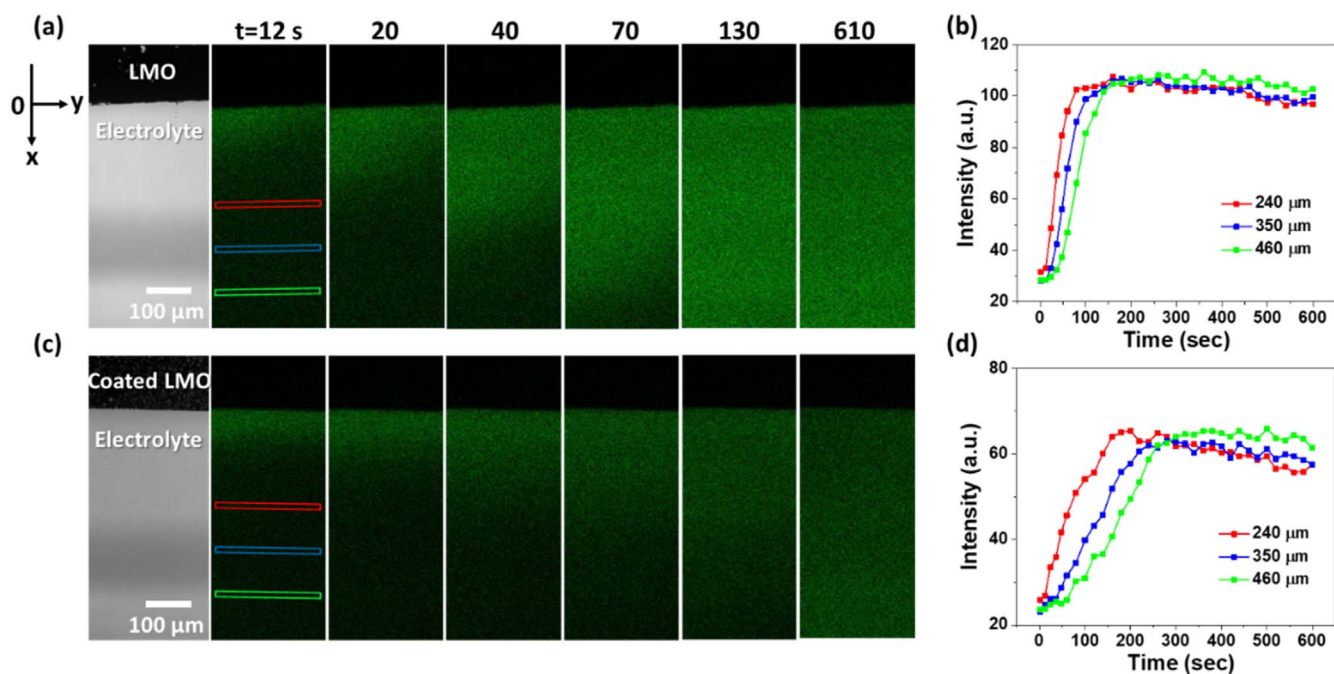


Fig. 4. Optical images and fluorescence images of (a) bare LMO and (c) Al₂O₃-coated LMO at various time spots. The regions used to determine fluorescence intensity as a function of time and location are shown as rectangles in images at $t = 12$ s. The electrode/electrolyte interface is set at a position of $0 \mu\text{m}$. (b and d) intensity vs. time of (b) bare LMO and (d) Al₂O₃-coated LMO at different locations.

emission spectroscopy and scanning electrochemical microscopy, since the former does not provide spatial resolution, and the latter operates at a time scale of 10^2 – 10^3 s, preventing the detection of ion concentration at different locations simultaneously. [46,47] Therefore, these results demonstrate the potential of fluorescence-based techniques to understand problems directly related to real batteries, as well as evaluate and develop battery materials. We believe that, with a wise choice of fluorescence indicators, this technology can be applied to systems including but not limited to the interaction between a solid electrode and liquid electrolyte, and ion transport in a liquid electrolyte that is either aqueous or non-aqueous. Moreover, it is even possible to extend to polymer electrolyte through incorporating dye into polymer or functionalizing polymer with dyes.

The above results demonstrate that fluorescence imaging can provide rich information about the temporal and spatial distribution of Mn^{2+} ions simultaneously, which is difficult to achieve by other approaches. To further explore the capability of this technique, modeling was carried out to extract quantitative information from observations, such as the ion diffusion coefficient and the dissolution rate of Mn^{2+} . One dimensional diffusion is assumed based on the sample geometry. First, the temporal evolution of fluorescence signals at certain distance away from the LMO/electrolyte interface was calculated as the average signal in rectangles for bare LMO (Fig. 4c) and Al₂O₃-coated LMO (Fig. 4d), respectively. The fluorescence intensity was converted to concentration based on the fitting curve at pH=5 in Fig. 2b. In conversion, it was assumed that the maximum and minimum intensities observed in imaging corresponded to dye saturated by Mn^{2+} and no Mn^{2+} , respectively. This assumption is valid since the ratio of LMO to electrolyte in samples for fluorescence imaging was ten times larger than that used in reader. Therefore, the dissolved Mn^{2+} in these samples was more than enough to saturate the dye in the solution.

Once the concentration profile of Mn^{2+} , $u(x, t)$, at each position and time was obtained, it was applied to the governing diffusion equations for simulation, which are:

$$\begin{cases} \frac{\partial}{\partial t}u(x, t) - D_{\text{sol}}\frac{\partial^2}{\partial x^2}u(x, t) = 0, & x \in (0, R), \quad t > 0 \\ \frac{\partial}{\partial t}u(x, t) - D_{\text{film}}\frac{\partial^2}{\partial x^2}u(x, t) = f, & x \in (-L, 0), \quad t > 0 \end{cases} \quad (1)$$

where D_{film} and D_{sol} are the diffusion coefficient of Mn^{2+} -dye complex inside the LMO film and in the electrolyte region, respectively. f is the dissolution rate of Mn^{2+} . Here D_{film} is assumed to be $0.5^{1/2} D_{\text{sol}}$ based on effective medium theory and a porosity of 50% [48,49]. As shown in Fig. S6, the interval $(0, R)$ denotes the electrolyte region, while $(-L, 0)$ indicates the LMO film region. In the simulation, we choose $R = L = 3000 \mu\text{m}$ which were large enough to approximate the wide region. Although the dissolution rate and the diffusion coefficients could be determined simultaneously from the observed concentration profile of Mn^{2+} , from computational point of view, it would be more convenient to identify a single parameter D_{sol} first, by assuming that f , the dissolution rate of Mn^{2+} , is a constant independent of x and t (see Supporting information for details).

To this end, we exploited the model (1) with a no-flux boundary condition $\frac{\partial}{\partial x}u(-L, t) = 0$, a zero boundary condition $u(R, t) = 0$, and a zero initial condition $u(x, 0) = 0$. Moreover, $u(x, t = 46 \text{ s}, 58 \text{ s}, 70 \text{ s})$ for both LMO and Al₂O₃-coated LMO were used for fitting. These times were selected because the concentration was high enough to avoid fluctuation in signal, but not too high to approach the saturated region, where the fluorescence signal is no longer sensitive to concentration change. As shown in Fig. 5a and b, when using a single D_{sol} for each sample at various times, the diffusion coefficients of $8.2 \times 10^{-6} \text{ cm}^2/\text{s}$ and $7.2 \times 10^{-6} \text{ cm}^2/\text{s}$ were derived for LMO and Al₂O₃-coated LMO, respectively. These values are consistent with CG-5N or other small-molecule dye [50,51], which is also similar to the diffusion coefficient of Mn^{2+} ion in water [52].

After D_{sol} was determined, it was then applied to compute the corresponding dissolution rate f . More details of the modeling can be found in the Supporting information. Here different f values were used for different times to account for the possible temporal variation of f (Fig. 5). The dissolution rates are quite similar at four time spots for LMO, changing from 2.0 to 1.8 and 1.7 $\mu\text{M}/\text{s}$, for from 46 s to 90 s. In comparison, the dissolution rate f of Al₂O₃-coated LMO, changes from

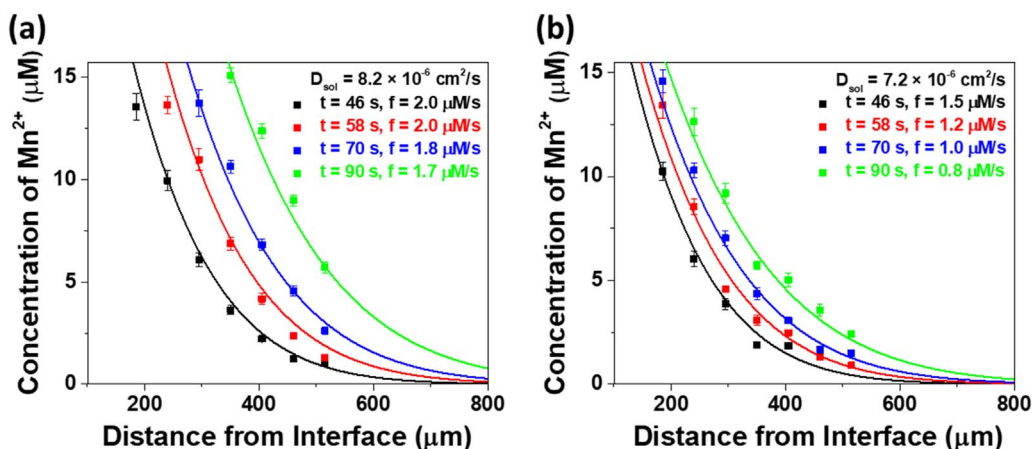


Fig. 5. Quantitative determination of ion diffusion coefficient and dissolution rate by modeling. Data points indicate $[\text{Mn}^{2+}]$ profile in the aqueous electrolyte at different times for (a) bare LMO and (b) Al_2O_3 -coated LMO. The solid line shows the fitted curve with a single diffusion coefficient (D_{sol}) and multiple dissolution rates (f) in diffusion model for data at all four time spots.

1.5 to 1.2, 1.0 and 0.8 $\mu\text{M/s}$, for from 46 s to 90 s, which is averagely 60% of bare LMO. The error in the fitted value of f was estimated to be 10% based on fitting with varied values (Fig. S7). Therefore, the observed difference in f was significant between bare and coated samples. These results show that Al_2O_3 indeed protected LMO and reduced dissolution remarkably, and are consistent with those from fluorometer in Fig. 2d. The fluctuation in f , especially for Al_2O_3 -coated one, possibly arises from time-dependent dissolution rate. Nevertheless, f for Al_2O_3 -coated one is always smaller than bare LMO. Moreover, the model gives diffusion coefficients under the two conditions, which are very close to one other and similar to the reported value of Mn-dye complex [50–52]. These results not only demonstrate that the model is self-consistent, but show that the fluorescence imaging can also act as a quantitative approach to extract useful physical information from battery systems. Studies on single particle-based dissolution and particle-to-particle variation will be carried out in the future to shed light on the heterogeneity of the dissolution process and potentially unveil approaches to enhance battery performance.

The observation that Al_2O_3 coating suppresses Mn dissolution is also supported by electrochemical measurements (Fig. 6). Both bare LMO and Al_2O_3 -coated LMO were tested in a standard coin cell configuration with organic electrolyte (1 M LiPF_6 in EC/DEC). All cells were cycled at C/5 (1 C = 148 mA/g) for first two cycles, followed by cycling at 1 C for the remaining cycles. The Al_2O_3 -coated LMO clearly shows a higher specific capacity at 60 °C than bare LMO (Fig. 6a and b), because less Mn is dissolved. At a rate of 1 C, the initial discharge specific capacity was 82 and 96 mA h/g for LMO and Al_2O_3 -coated LMO cells, respectively, and the specific capacity remained at 70 and 80 mA h/g after 50 cycles. The higher capacity of Al_2O_3 -coated LMO suggests that there is less dissolution of Mn^{2+} from it. Moreover, Al_2O_3 -coated LMO shows an

average Coulombic efficiency of 98.9% between the 3rd and 50th cycle, higher than that of bare LMO (98.0%), as shown in Fig. 6c. The difference in CE suggests that the side reaction is reduced to about half when Al_2O_3 coating is applied, which also supports the reduction in Mn dissolution.

4. Conclusion

In summary, the dissolution of Mn^{2+} from LMO in aqueous acidic solution was visualized by fluorescence imaging for the first time. The temporal and spatial evolution of trace amount of Mn^{2+} (< 10 μM) dissolved from LMO could be visualized by this technique, and observed results are quantitatively consistent with modeling. This work shows that fluorescence imaging is a powerful tool to understand processes in battery systems, such as the interaction between a solid electrode and liquid electrolyte, ion transport in a liquid electrolyte or even solid polymer electrolyte, etc. Such capability is difficult to achieve by other means. Consequently, we believe fluorescence imaging is a promising technique for a diversity of applications, such as investigating ion transport within membranes (e.g., Nafion, nonperfluorinated polymer membranes, etc.) or the interaction between a membrane and liquid electrolyte in vanadium flow battery, and visualizing multiple ion dissolution simultaneously in high-nickel ternary cathode materials with a smart choice of fluorescent indicators. Notably, this work is not an in-situ experiment yet, which is a quite challenging task and requires more efforts in the future. As fluorescence imaging technology is rapidly evolving along several directions, especially developing specific ion indicators applicable in organic electrolytes, we believe fluorescence imaging can help unveil miscellaneous phenomena in battery systems and develop better battery materials.

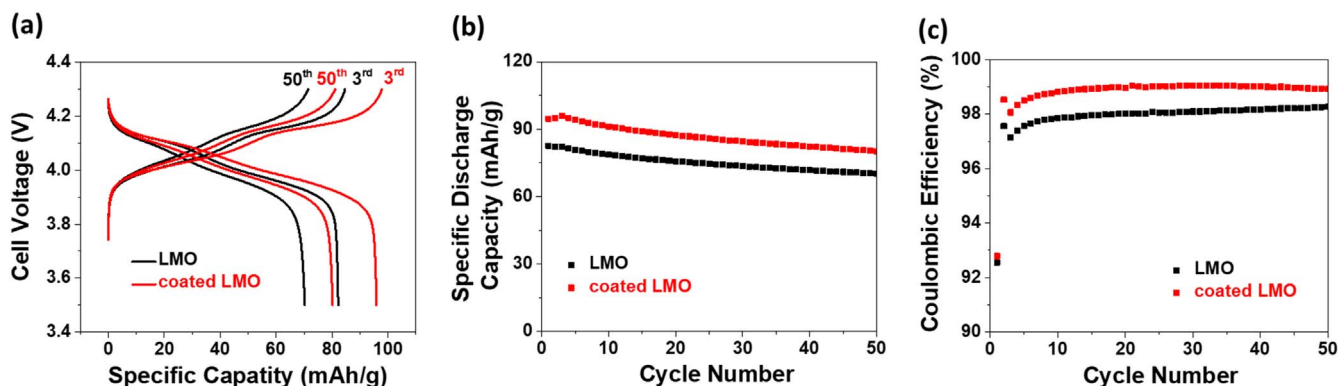


Fig. 6. Electrochemical performance of LMO/Li and Al_2O_3 -coated LMO/Li half-cells. The cell is charged/discharged at C/5 (29.6 mA/g) for the first two cycles and 1 C for the remaining cycles. (a) Voltage profiles of the 3rd and 50th charge/discharge cycle. The 3rd cycle corresponds to the 1st cycle at 1 C rate. (b) Cycling performance, and (c) Coulombic efficiency of cells with bare LMO and Al_2O_3 -coated LMO as cathodes.

Acknowledgment

Y. Y. acknowledges support for startup funds from Columbia University and seed fund from Lenfest Center for Sustainable Energy at Columbia University. We acknowledge seed funding support from Columbia University's Research Initiatives in Science & Engineering competition, started in 2004 to trigger high-risk, high-reward, and innovative collaborations in the basic sciences, engineering, and medicine. This work is supported by the NSF MRSEC program through Columbia in the Center for Precision Assembly of Superstratic and Superatomic Solids (DMR-1420634). The research of Q. D. is supported in part by NSF DMS 1719699 and ARO MURI Grant W911NF-15-1-0562. The research of Z. Z. is partially supported by startup funds from Hong Kong Polytechnic University.

Appendix A. Supporting information

Supplementary data associated with this article can be found in the online version at <http://dx.doi.org/10.1016/j.nanoen.2017.12.036>.

References

- [1] S. Chu, Y. Cui, N. Liu, *Nat. Mater.* 16 (2017) 16–22.
- [2] W. Liu, M.-S. Song, B. Kong, Y. Cui, *Adv. Mater.* 29 (2017) 1603436.
- [3] S. Chu, A. Majumdar, *Nature* 488 (2012) 294–303.
- [4] M.S. Whittingham, *MRS Bull.* 33 (2011) 411–419.
- [5] J. Lu, T. Wu, K. Amine, *Nat. Energy* 2 (2017) 17011.
- [6] J. Lim, Y. Li, D.H. Alsem, H. So, S.C. Lee, P. Bai, D.A. Cogswell, X. Liu, N. Jin, Y.-s. Yu, N.J. Salmon, D.A. Shapiro, M.Z. Bazant, T. Tylliszczak, W.C. Chueh, *Science* 353 (2016) 566–571.
- [7] J. Nelson, S. Misra, Y. Yang, A. Jackson, Y. Liu, H. Wang, H. Dai, J.C. Andrews, Y. Cui, M.F. Toney, *J. Am. Chem. Soc.* 134 (2012) 6337–6343.
- [8] H. Liu, F.C. Strobridge, O.J. Borkiewicz, K.M. Wiaderek, K.W. Chapman, P.J. Chupas, C.P. Grey, *Science* 344 (2014) 1252817.
- [9] J. Conder, R. Bouchet, S. Trabesinger, C. Marino, L. Gubler, C. Villevieille, *Nat. Energy* 2 (2017) 17069.
- [10] M.R. Lukatskaya, S.-M. Bak, X. Yu, X.-Q. Yang, M.W. Barsoum, Y. Gogotsi, *Adv. Energy Mater.* 5 (2015) 1500589.
- [11] X. Yu, H. Pan, Y. Zhou, P. Northrup, J. Xiao, S. Bak, M. Liu, K.-W. Nam, D. Qu, J. Liu, T. Wu, X.-Q. Yang, *Adv. Energy Mater.* 5 (2015) 1500072.
- [12] W.-S. Yoon, O. Haas, S. Muhammad, H. Kim, W. Lee, D. Kim, D.A. Fischer, C. Jaye, X.-Q. Yang, M. Balasubramanian, K.-W. Nam, *Sci. Rep.* 4 (2014) 6827.
- [13] J.Y. Huang, L. Zhong, C.M. Wang, J.P. Sullivan, W. Xu, L.Q. Zhang, S.X. Mao, N.S. Hudak, X.H. Liu, A. Subramanian, H. Fan, L. Qi, A. Kushima, J. Li, *Science* 330 (2010) 1515–1520.
- [14] M.T. McDowell, Z. Lu, K.J. Koski, J.H. Yu, G. Zheng, Y. Cui, *Nano Lett.* 15 (2015) 1264–1271.
- [15] M. Gu, L.R. Parent, B.L. Mehdi, R.R. Unocic, M.T. McDowell, R.L. Sacci, W. Xu, J.G. Connell, P. Xu, P. Abellan, X. Chen, Y. Zhang, D.E. Perea, J.E. Evans, L.J. Lauhon, J.-G. Zhang, J. Liu, N.D. Browning, Y. Cui, I. Arslan, C.-M. Wang, *Nano Lett.* 13 (2013) 6106–6112.
- [16] M.T. McDowell, I. Ryu, S.W. Lee, C. Wang, W.D. Nix, Y. Cui, *Adv. Mater.* 24 (2012) 6034–6041.
- [17] E. Ventosa, W. Schuhmann, *Phys. Chem. Chem. Phys.* 17 (2015) 28441–28450.
- [18] P. Bertoncello, *Energy Environ. Sci.* 3 (2010) 1620–1633.
- [19] N. Balke, S. Jesse, A.N. Morozovska, E. Eliseev, D.W. Chung, Y. Kim, L. Adamczyk, R.E. Garcia, N. Dudney, S.V. Kalinin, *Nat. Nanotechnol.* 5 (2010) 749–754.
- [20] N.A. Padilla, M.T. Rea, M. Foy, S.P. Upadhyay, K.A. Desrochers, T. Derus, K.A. Knapper, N.H. Hunter, S. Wood, D.A. Hinton, A.C. Cavell, A.G. Masias, R.H. Goldsmith, *ACS Sens.* 2 (2017) 903–908.
- [21] X.-B. Cheng, R. Zhang, C.-Z. Zhao, F. Wei, J.-G. Zhang, Q. Zhang, *Adv. Sci.* 3 (2016) 1500213.
- [22] C.G. Galbraith, J.A. Galbraith, *J. Cell Sci.* 124 (2011) 1607–1611.
- [23] B. Huang, M. Bates, X. Zhuang, *Annu. Rev. Biochem.* 78 (2009) 993–1016.
- [24] B.A. Wilt, L.D. Burns, E.T.W. Ho, K.K. Ghosh, E.A. Mukamel, M.J. Schnitzer, *Annu. Rev. Neurosci.* 32 (2009) 435–506.
- [25] Y. Zhang, J.M. Lucas, P. Song, B. Beberwyck, Q. Fu, W. Xu, A.P. Alivisatos, *Proc. Natl. Acad. Sci. USA* 112 (2015) 8959–8964.
- [26] P. Chen, X. Zhou, N.M. Andoy, K.-S. Han, E. Choudhary, N. Zou, G. Chen, H. Shen, *Chem. Soc. Rev.* 43 (2014) 1107–1117.
- [27] Z.M. Dang, J.K. Yuan, J.W. Zha, T. Zhou, S.T. Li, G.H. Hu, *Prog. Mater. Sci.* 57 (2012) 660–723.
- [28] A. Jarry, S. Gottis, Y.-S. Yu, J. Roque-Rosell, C. Kim, J. Cabana, J. Kerr, R. Kostecki, *J. Am. Chem. Soc.* 137 (2015) 3533–3539.
- [29] L. Zhao, E. Chenard, N.R. Sottos, S.R. White, *Meet. Abstr. No. 2*, The Electrochemical Society, 2017.
- [30] Z. Guo, L. Chen, Y. Wang, C. Wang, Y. Xia, *ACS Sustain. Chem. Eng.* 5 (2017) 1503–1508.
- [31] X. Dong, L. Chen, X. Su, Y. Wang, Y. Xia, *Angew. Chem. Int. Ed.* 55 (2016) 7474–7477.
- [32] Y. Wang, L. Chen, Y. Wang, Y. Xia, *Electrochim. Acta* 173 (2015) 178–183.
- [33] X. Wang, Y. Hou, Y. Zhu, Y. Wu, R. Holze, *Sci. Rep.* 3 (2013) 1401.
- [34] J. Lu, C. Zhan, T. Wu, J. Wen, Y. Lei, A.J. Kropf, H. Wu, D.J. Miller, J.W. Elam, Y.-K. Sun, X. Qiu, K. Amine, *Nat. Commun.* 5 (2014) 5693.
- [35] R.J. Gummow, A. de Kock, M.M. Thackeray, *Solid State Ion.* 69 (1994) 59–67.
- [36] D. Guyomard, J.M. Tarascon, *J. Electrochem. Soc.* 139 (1992) 937–948.
- [37] M.M. Thackeray, W.L.F. David, P.G. Bruce, J.B. Goodenough, *Mater. Res. Bull.* 18 (1983) 461–472.
- [38] C. Zhan, J. Lu, A. Jeremy Kropf, T. Wu, A.N. Jansen, Y.-K. Sun, X. Qiu, K. Amine, *Nat. Commun.* 4 (2013) 2437.
- [39] L. Yu, X. Qiu, J. Xi, W. Zhu, L. Chen, *Electrochim. Acta* 51 (2006) 6406–6411.
- [40] G.G. Amatucci, C.N. Schmutz, A. Blyr, C. Sigala, A.S. Gozdz, D. Larcher, J.M. Tarascon, *J. Power Sources* 69 (1997) 11–25.
- [41] C.C.R. Sutton, G.V. Franks, G. da Silva, *J. Phys. Chem. B* 116 (2012) 11999–12006.
- [42] J. Liang, J.W. Canary, *Angew. Chem. Int. Ed.* 49 (2010) 7710–7713.
- [43] C.R.R. Gan, Z. Liu, S.-Q. Bai, K.S. Ong, T.S.A. Hor, *Dalton Trans.* 43 (2014) 1821–1828.
- [44] F. Lai, X. Zhang, H. Wang, S. Hu, X. Wu, Q. Wu, Y. Huang, Z. He, Q. Li, *ACS Appl. Mater. Interfaces* 8 (2016) 21656–21665.
- [45] J. Zhao, Y. Wang, *J. Solid State Electrochem.* 17 (2013) 1049–1058.
- [46] D. Polcari, P. Dauphin-Ducharme, J. Mauzeroll, *Chem. Rev.* 116 (2016) 13234–13278.
- [47] Y. Takahashi, A. Kumatani, H. Shiku, T. Matsue, *Anal. Chem.* 89 (2017) 342–357.
- [48] I.V. Thorat, D.E. Stephenson, N.A. Zacharias, K. Zaghib, J.N. Harb, D.R. Wheeler, *J. Power Sources* 188 (2009) 592–600.
- [49] D.A.G. Bruggeman, *Ann. Phys. (Berl.)* 416 (1935) 636–664.
- [50] C.T. Culbertson, S.C. Jacobson, J. Michael Ramsey, *Talanta* 56 (2002) 365–373.
- [51] P.O. Gendron, F. Avaltroni, K.J. Wilkinson, *J. Fluoresc.* 18 (2008) 1093–1101.
- [52] S.F. Patil, N.S. Rajurkar, A.V. Borhade, *J. Chem. Soc. Faraday Trans.* 87 (1991) 3405–3407.